RESEARCH ARTICLE | MAY 02 2023

Wake dynamic characteristics of windproof structures in embankment–bridge sections along a high-speed railway under natural strong crosswinds

Deng E (邓锷) (iD) ; Yue Huan (岳欢) (iD) ; Ni Yi-Qing (倪一清) ✉ (iD) ; He Xu-Hui (何旭辉);
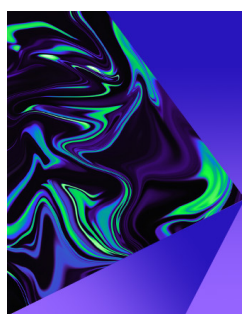Yang Wei-Chao (杨伟超); Chen Zheng-Wei (陈争卫) (iD)

🔴 Check for updates

View Online

Export Citation

Physics of Fluids

Special Topic:
Selected Papers from the 2023 Non-Newtonian
Fluid Mechanics Symposium in China

Submit Today

AIP Publishing

AIP Publishing

Wake dynamic characteristics of windproof structures in embankment–bridge sections along a high-speed railway under natural strong crosswinds

View Online   Export Citation   CrossMark

E Deng (邓锷),[1,2] Huan Yue (岳欢),[3] Yi-Qing Ni (倪一清),[1,2,a] Xu-Hui He (何旭辉),[3,4] Wei-Chao Yang (杨伟超),[3,4] and Zheng-Wei Chen (陈争卫)[1,2]

AFFILIATIONS

[1]National Rail Transit Electrification and Automation Engineering Technology Research Center (Hong Kong Branch), Hong Kong, China
[2]Department of Civil and Environmental Engineering, The Hong Kong Polytechnic University, Hong Kong, China
[3]School of Civil Engineering, Central South University, Changsha, China
[4]National Engineering Research Center of High-Speed Railway Construction Technology, Changsha, China

[a]Author to whom correspondence should be addressed: ceyqni@polyu.edu.hk

ABSTRACT

A recent trend in railway development around the world is the extension of high-speed railways to areas with harsh climatic environments. The aerodynamic performance of high-speed trains deteriorates when they run through embankment–bridge sections in a windy environment, posing potential safety risks. The present study aims to reveal the evolution mechanism of wake field in the transition section of the windbreak wall and wind barrier under natural strong crosswinds. First, the fluctuating characteristics of natural wind field collected by ultrasonic anemometers during a period of strong wind are captured. Next, the improved delayed detached eddy simulation scheme combined with the shear stress transfer $k–w$ model is used to elucidate the difference of flow field modes on the leeward side of the windproof structure in the transition section under the conditions of constant and fluctuating crosswinds. Finally, the effects of model scale ratio (1:20, 1:10, and 1:1) on wind field simulation results on the leeward side of the windproof structure are revealed. Results show that the incoming flow with time-varying velocity evokes the instability of wake vortices of the windbreak wall in the embankment. The transient evolution results of the vortices obtained by the 1:10 model are in good agreement with those of the 1:1 model, whereas the results obtained by the 1:20 model have a large deviation.

I. INTRODUCTION

With the booming development of high-speed rail, railway lines are bound to reach out to areas with harsh climate environments, such as the Lanzhou–Urumqi high-speed railway across China's windy northwest. China's terrain is undulating, and high-speed railway lines often need to cross mountains and valleys. A large number of tunnels and bridges have been built. According to statistics, bridges and tunnels along the high-speed railway in northwest China account for more than 80% (Yang et al., 2022a; He and Li, 2020; and He and Zhou, 2021). The wind direction in the windy area of Northwest China is usually single, so single-sided solid windbreak wall on the windward side of the embankment can achieve well windproof effect. However, in order to ensure the balance of the bridge, wind barriers need to be set on both sides of the bridge (Gu et al., 2020). To ensure the running safety of trains in windy areas, various forms of windproof structures have been applied along high-speed railways, e.g., concrete windbreak walls on embankments and porous wind barriers on bridges. Most of the railway windproof structures can offer favorable shelter effects against strong incoming crosswind flow. However, the aerodynamic performance of high-speed trains (HSTs) deteriorates when they pass through the transition section of a windproof structure, thus posing potential safety risks (Gao et al., 2021, Wei et al., 2022).

Elucidating the evolution characteristics of the wake vortex structure on the leeward side of the windproof structure in this transition section is necessary to reveal the deterioration mechanism of the aerodynamic performance of HSTs. Field test of the wind field outside the windproof structure is easy, whereas the wind field inside the windproof structure is difficult to monitor when the railway line is in normal operation. In order to explore the reasons for the deterioration of the aerodynamic performance of the train, the study monitored the wind field on the windward side of the line and then combined the computational fluid dynamics (CFD) numerical simulation method to predict the wind field characteristics on the embankment–bridge section.

Numerous researchers have conducted investigations on the flow field characteristics of the leeward side of windproof structures on the flat grounds, embankments, and bridges under a strong wind environment. Niu *et al.* (2018a) compared the aerodynamic performance of trains with and without a windbreak wall on an embankment under the action of crosswind by means of delayed detached eddy simulation (DDES). Subsequently, they Niu *et al.* (2022) investigated the effects of single and double windbreak walls on the aerodynamic loads of HSTs running on the windward and leeward lines in a crosswind environment. The results showed that the two-side windbreak walls have different effects on the unsteady aerodynamic loads of trains running on the windward and leeward lines. Making use of the lattice Boltzmann method, Masoud *et al.* (2019) conducted a study on the influence of the height and porosity of a railway porous windbreak wall founded on flat ground on its windproof performance. The results showed that the windbreak wall with 15% porosity can remarkably reduce the deterioration of aerodynamic performance of trains caused by the kinetic energy of incoming crosswind. Hashmi *et al.* (2019) studied for the first time the influence of different types of windbreak wall transition sections on the surface pressure of trains based on wind tunnel tests. Liu *et al.* (2018) and Chen and Ni (2022a) combined field tests and computational fluid dynamics (CFD) simulation to reveal the relationship between the deterioration of HST running safety and the sudden change boundary of the windbreak wall in windy areas. In contrast to embankments, wind barrier structures of bridges are usually ventilated to seek a compromise between windproof performance and wind load reduction. Kozmar *et al.* (2014) studied the influence of the porosity and height of a wind barrier of a bridge on the average velocity field and vorticity field of the leeward side by using the particle image velocimetry technique. He *et al.* (2019) investigated the aerodynamic effect of a new louver-type wind barrier on a train–bridge system via wind tunnel tests. Gu *et al.* (2020) combined wind tunnel test and CFD simulation to study the variation of flow field structure on the leeward side of a corrugated wind barrier on a bridge and its shielding performance for HSTs under crosswinds. A difference is often observed between the windproof structure on embankments and that on bridges, and all kinds of semi-enclosed windproof structures cannot completely protect HSTs from the interference of crosswind flow. However, the flow field on the leeward side of the windproof structure in the embankment–bridge transition section was often ignored by researchers.

The establishment of incoming flow conditions is essential to the simulation of windy environment. The previous studies have mainly focused on constant wind velocity conditions. For example, Telenta *et al.* (2014) and Xu *et al.* (2022) studied the flow characteristics of

turbulent wakes on the leeward side of a wind barrier with different openings under the constant crosswind condition by using the unsteady Reynolds-averaged Navier–Stokes CFD method. Bendjebbas *et al.* (2018) used the COMSOL Multiphysics® software to study the influence of a wind barrier on the flow around the heliostat on the leeward side under the atmospheric boundary layer (ABL) incoming flow with constant wind velocity. Based on CFD simulation and on-site measurements, Dong *et al.* (2021) studied the influence law of the porosity of the windbreak wall of an embankment on the dynamic response of the leeward catenary under the condition of ABL crosswind flow with constant wind velocity. Several researchers have paid attention to the influence of incoming flow with time-varying wind velocity on the wake vortex of target objects. For example, Chen *et al.* (2022b) used the synthetic eddy method embedded in CFD to generate three incoming turbulence modes, studying the difference in dynamic characteristics of wind turbine wake vortices under different incoming flow conditions and revealing the influence of fluctuating incoming wind on the wake vortex shedding law of wind turbine blades. Various simulation methods for fluctuating wind field have been proposed; for example, Li *et al.* (2017) and Hu *et al.* (2019) proposed a set of fluctuating flow generation methods for moving trains on the basis of the empirical wind power spectrum. However, the wind field simulation methods in these studies deviate from the characteristics of natural wind field to a certain extent.

Some researchers adopted scale models to study the dynamic evolution characteristics of wake vortices around target objects under the condition of fluctuating incoming flow. For example, Niu *et al.* (2017) used a wind tunnel test scheme with a scale ratio of 1:8 to observe the influence of the turbulence intensity of incoming flow on the aerodynamic pressure fluctuation characteristics of a train model. The results showed that the turbulent incoming flow leads to a premature reattachment of the shear layer on the train surface. Noguchi *et al.* (2019) used a wind tunnel model with a scale ratio of 1:40 to test the aerodynamic coefficient of a carriage on embankment under ABL incoming flow. Chen *et al.* (2020) used a CFD model with a scale ratio of 1:10 to compare the difference of flow field on the leeward side of a railway windbreak wall near a mountain ridge under two inlet boundary conditions (uniform and ABL). Niu *et al.* (2018b) compared the CFD simulation results of train–tunnel models with different scaling ratios and found that the thickness of the boundary layer on the train surface increases with the reduction of the model scale, thus affecting the computational results of the pressure on the train surface to a certain extent. However, no study was reported about the effect of scale Reynolds effect on the dynamic characteristics of wake on the leeward side of windproof structures under crosswinds.

In this paper, the embankment–bridge transition section along a typical high-speed railway line in northwest China is taken as a testbed to investigate its wake dynamic characteristics under crosswinds. First, the spectral coherence characteristics of the wind field collected by ultrasonic anemometers during a period of strong wind are captured. Then, the measured time-history samples of wind velocity are used as incoming flow boundary conditions for CFD simulation. The improved DDES (IDDES) scheme combined with the shear stress transfer k–w (SST k–w) model is employed to elucidate the difference of flow field modes on the leeward side of a windproof structure in the transition section under the conditions of constant and fluctuating crosswinds. Finally, the effects of model scale ratio (1:20, 1:10, and 1:1)

on the wind field simulation results of the leeward side of the wind-proof structure are revealed. The primary contributions of this study include: (1) elucidation of the influence mechanism of natural fluctuating incoming flow on the shedding of leeward vortex of solid windbreak wall and porous wind barrier, and (2) development of a procedure for predicting the wake flow field of windproof structures by adopting a reasonably reduced scale CFD model. (3) The study provides scientific evidence for the design of windproof facilities in embankment–bridge section along high-speed railway. (4) The Reynolds number effect between different scale models is studied to provide guidance for wind tunnel experiments.

II. FIELD TEST

A. Site overview and layout of measuring points

The test site is in the core of the Baili wind zone in northwest China, as shown in Fig. 1. Local meteorological data show that the wind in this area is strong all year round (the highest instantaneous wind velocity reaches up to 60 m/s), and the wind direction is relatively stable, mainly from the north. The high-speed railway section at the test site basically runs east–west, about 5° south by west. The embankment section is located on the east side, while the bridge section is situated on the west side. The type of windproof facilities in the embankment section is single-sided solid windbreak wall with a height of about 5.2 m. The double-side porous barrier installed on the bridge section is about 4.2 m high, and the porosity is 30%.

As shown in Fig. 2, three ultrasonic anemometers (3-axis, Gill Wind Master Pro, sampling frequency: 32 Hz) were arranged side by side on the flat ground on the windward side of the high-speed rail line by a wind detector tower. Each tower was anchored to the ground by three anchor cables to ensure that the sensor's pointing needle is strictly north of the geographical direction and does not shake with the increase in wind velocity. The measuring points were numbered as #1, #2, and #3 from east to west. The height of the measuring points is 5 m above the ground, and the perpendicular distance from the rail line center is about 50 m. The model of the data acquisition system is Campbell CR6, which was positioned near measuring point #2 and was continuously powered by a 12-V battery.

B. Data processing

Given that the wind velocity component in the vertical line (perpendicular) direction on the horizontal plane is mainly concerned, the positive direction of wind velocity is designated as the vertical line and
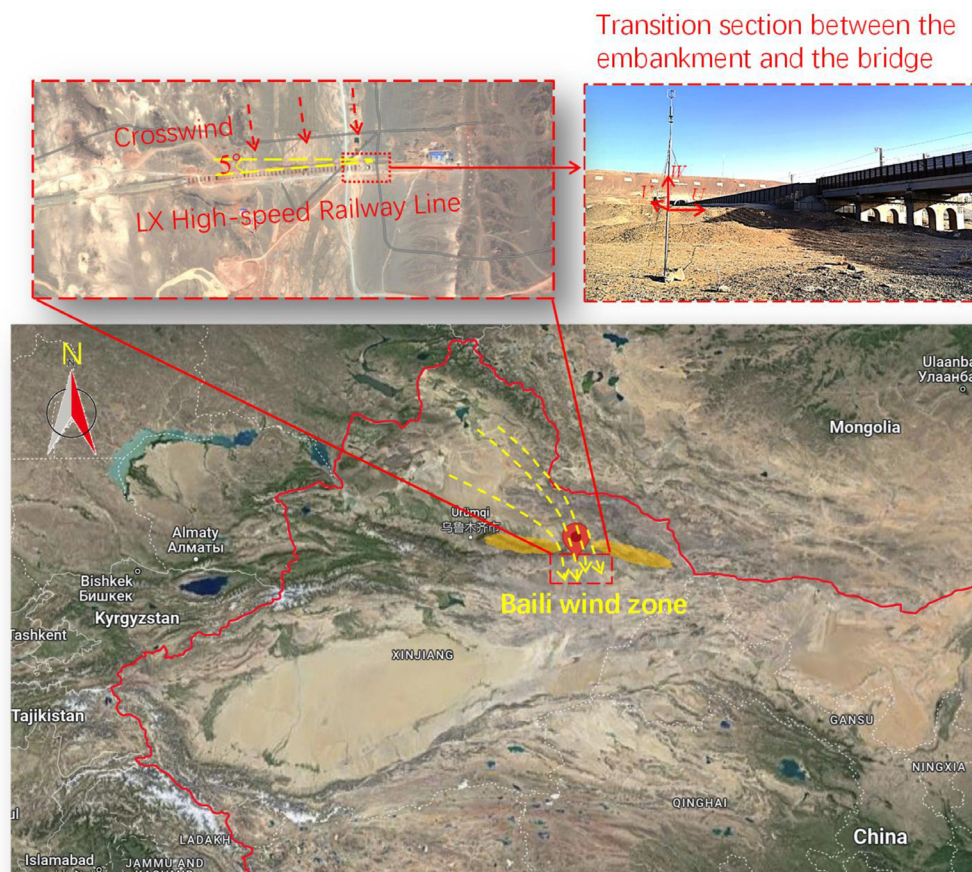
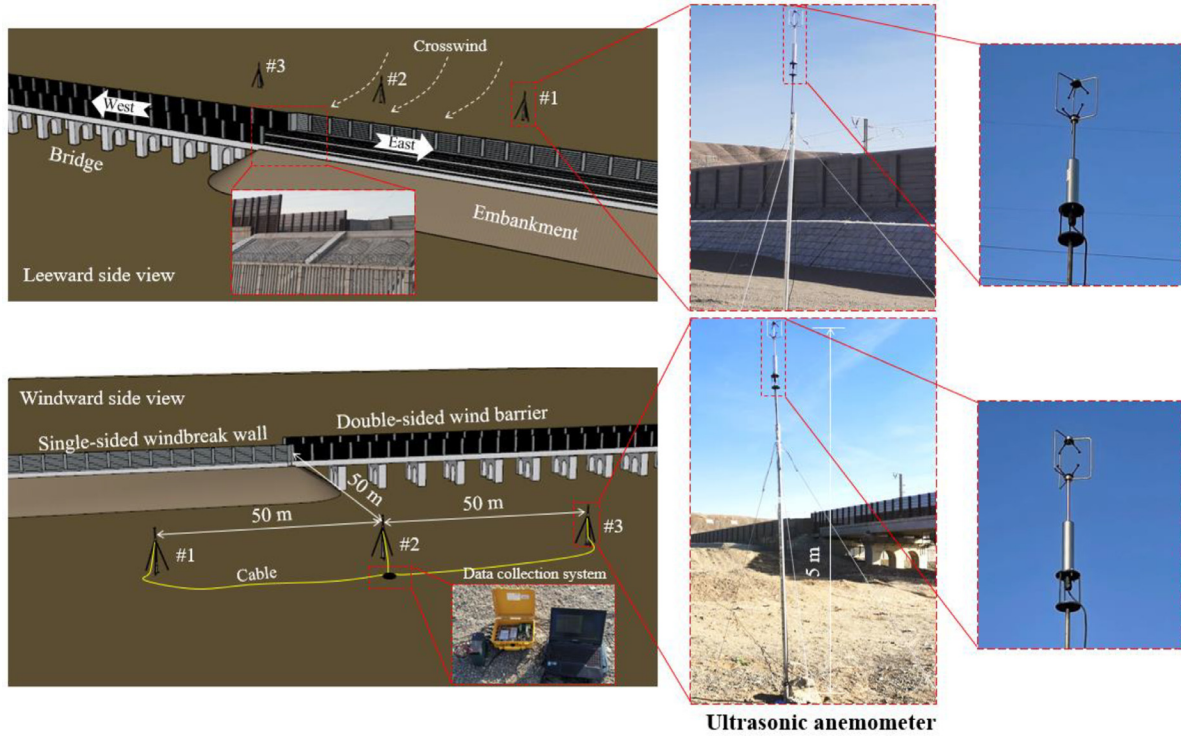

FIG. 1. Location of field test.

FIG. 2. On-site layout of measuring points.

pointed south (Fig. 3). The raw data collected by each ultrasonic anemometer include the horizontal wind velocity U_H, the horizontal wind direction angle θ, and the vertical wind velocity U_w. To obtain the wind velocity components U_u and U_v in the directions of u and v, the resultant wind velocity U_H is decomposed on the horizontal plane by using the following formulas:

$$\begin{cases} U_u = U_H \cos(\theta_0 - \theta), \\ U_v = U_H \sin(\theta_0 - \theta), \end{cases} \qquad (1)$$

where θ is the wind direction angle corresponding to the resultant wind velocity on the horizontal plane; its value ranges from $0°$ to $359.5°$, where $0°$ denotes the direction of due north and the angle increases clockwise. θ_0 is the direction wind angle ($355°$).

An eight-carriage HST running at normal speed takes less than 3 s to cross the embankment–bridge junction. Therefore, when calculating the average wind velocity and turbulence intensity, a 3 s time interval was adopted to segment the time-history samples of wind velocity. The formulas for calculating average wind velocity and turbulence intensity of the U component of each sample are as follows:

$$\overline{U_u} = \sum_{i=1}^{n} U_{ui}/n, \qquad (2)$$

$$I_u = \frac{\sqrt{\sum_{i=1}^{n}(U_{ui} - \overline{U_u})^2/n - 1}}{\sum_{i=1}^{n}\sqrt{U_{Hi}^2 + U_{wi}^2}/n}, \qquad (3)$$

where n is the number of data points on a component of wind velocity at a measuring point within a 3 s time interval, and its value is 96.
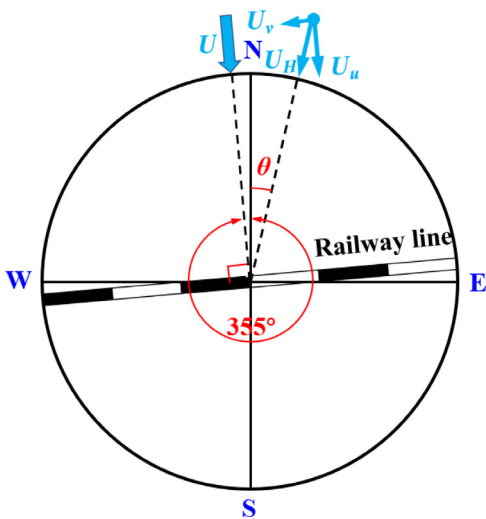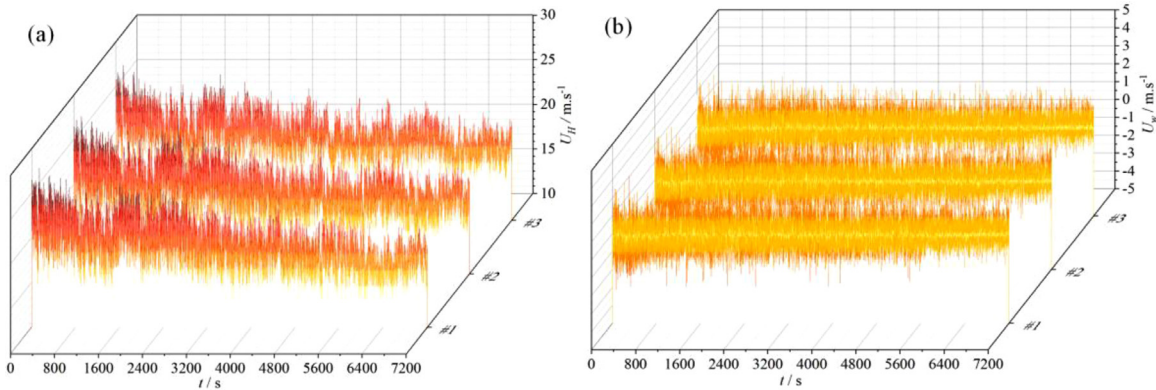

FIG. 3. Diagram of wind velocity decomposition.

FIG. 4. Time-history curves of wind velocity lasting 2 h: (a) horizontal H component and (b) W component.

C. Result analysis

1. Wind velocity and direction

During the test, each anemometer recorded a complete sample of strong winds lasting for 2 h. Figure 4 shows the time-history curves of wind velocity at the three measuring points, and Fig. 5 shows the corresponding rose diagrams of wind direction.

It is seen from Fig. 4 that the fluctuations of wind velocity at the three measuring points are quite consistent. The fluctuation of wind velocity in the first half of the duration is violent, with the highest instantaneous wind velocity reaching up to 27 m/s; the wind velocity fluctuation in the latter half of the duration is relatively weak. The W component of wind velocity at the three measuring points fluctuates slightly around zero value. The wind field in this area exhibits remarkable two-dimensional characteristics. Furthermore, it is observed from Fig. 5 that the wind direction of incoming flow at the three measuring points is consistent and stable. The mainstream direction is nearly perpendicular to the railway line, and the angle between it and the U direction is kept within 5°, indicating that the U component of wind velocity can approximately represent the resultant wind velocity at each measuring point. For convenience of analysis, the subsequent work will focus only on the U component.

To characterize the correlation of wind velocity between adjacent measuring points quantitatively, Fig. 6 shows the curve fitting results on the correlation of 3 s samples of the U component of wind velocity between the adjacent measuring points. As shown in Fig. 6, the slopes of the two fitted curves between #1 and #2 and between #2 and #3 are both close to 1, and the sample points converge to the fitted curves with the increase in wind velocity. This indicates that the U component of wind velocity between the adjacent measuring points holds a high degree of correlation, and the wind velocity samples collected at the measuring points are representative.

2. Turbulence characteristics

Figure 7 shows the relationship between the turbulence intensity of the U component and the corresponding 3 s average wind velocity at three measuring points. It is seen that the distribution patterns of turbulence intensity samples at the three measuring points are similar, and the slopes of the external envelope are the same. When wind velocity is low, the turbulence intensity samples are scattered, and the maximum value of the turbulence intensity is 0.16. With the increase in wind velocity, the turbulence intensity tends to be a fixed value. The trend value is 0.04 for points #1 and #2 and about 0.03 for point #3.
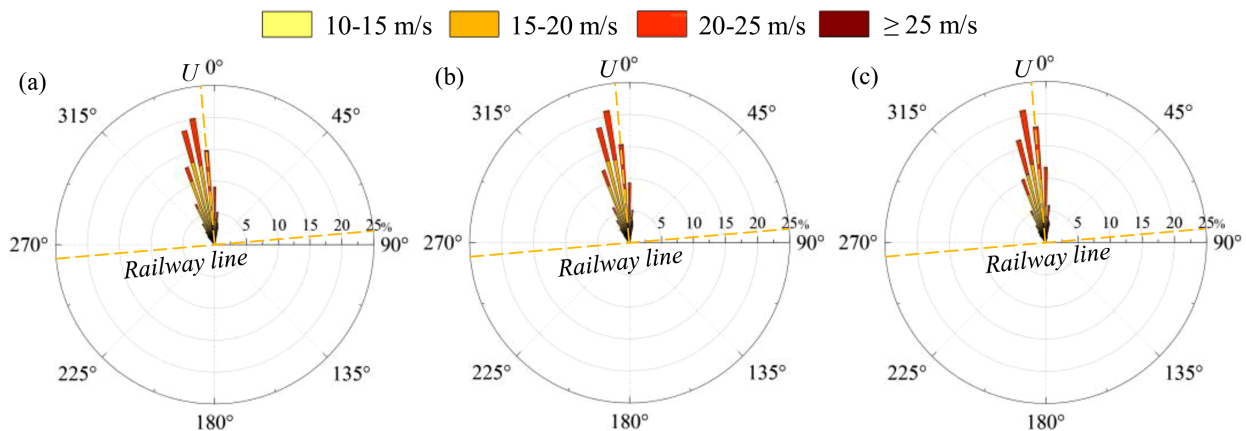

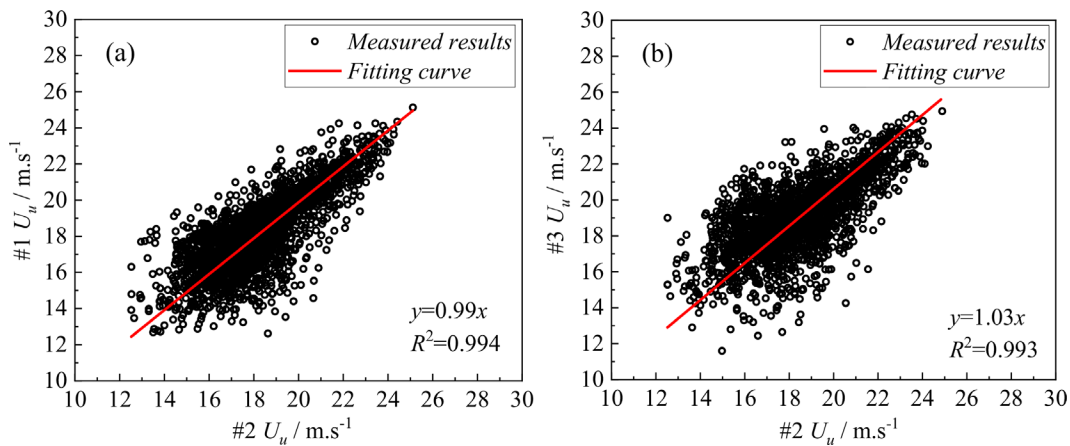**FIG. 5.** Rose diagrams of wind direction: (a) #1; (b) #2; and (c) #3.

FIG. 6. U component wind velocity correlation between adjacent measuring points: (a) #1 and #2; (b) #2 and #3.
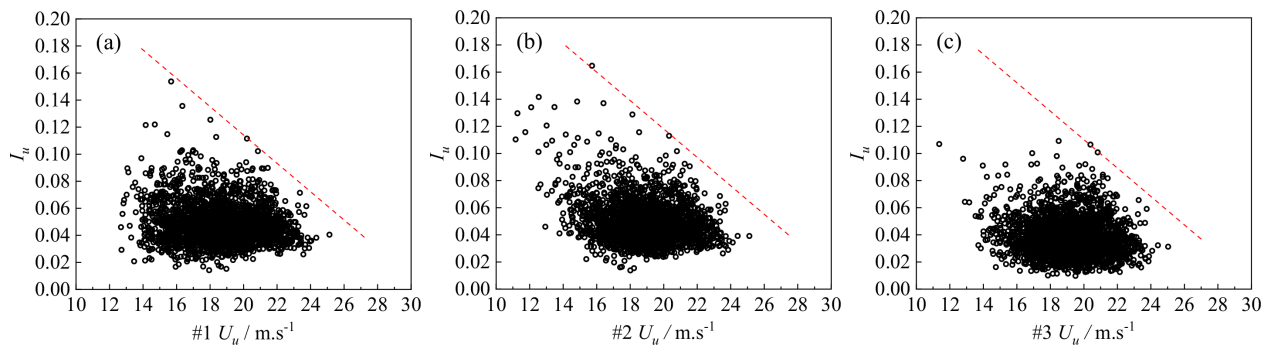

FIG. 7. Scatter plot of turbulence intensity vs wind velocity: (a) #1; (b) #2; and (c) #3.

3. Power spectral density (PSD)

With the wind velocity samples in Fig. 4, the wind power spectral densities (PSDs) of the time-varying U component at three measuring points and the corresponding average integral scale are obtained by the Yule method (10th order, NFFT = 10 240), as shown in Fig. 8. It is found that the morphological characteristics of the time-varying PSD plane on the U component at the three measuring points are highly consistent. In the frequency domain, the value of PSD decreases monotonically with the increase in frequency, and the dominant frequency is about 0.008 Hz. In the time domain, the value of PSD is stable, and the peak value decreases slightly with time. The average integral scale of the wind field on the U component at the three
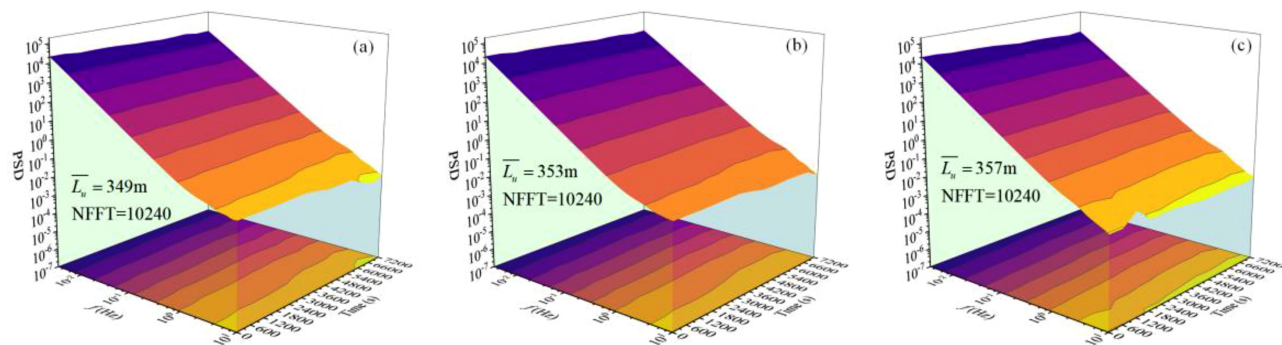

FIG. 8. Time-varying U component wind PSD: (a) #1; (b) #2; and (c)#3.
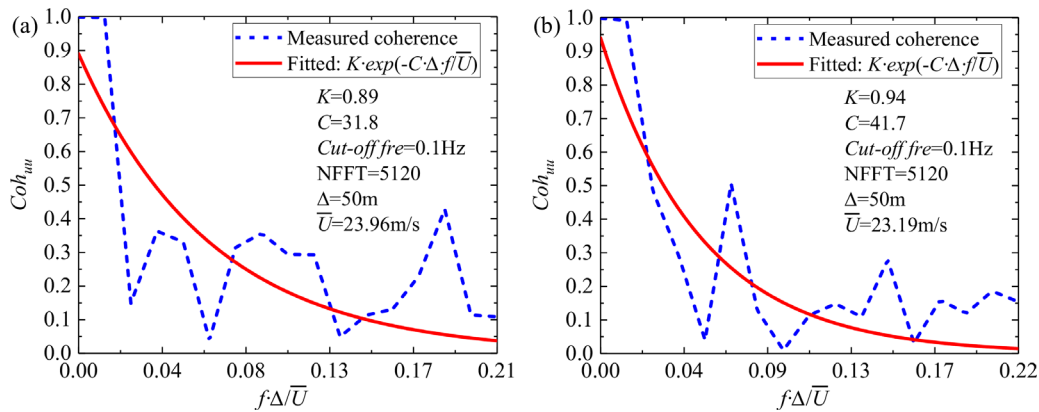
FIG. 9. Spectral coherence of the U component between two adjacent measuring points and its fitted curves: (a) #1 and #2 and (b) #2 and #3.

measuring points is maintained around 350 m, which is about 70 times that of the height of the windbreak wall.

To capture the spectral coherence of the U component between adjacent measuring points, 10 min consecutive PSD samples from the three measuring points in the same period with the highest average wind velocity are extracted, and then the *mscohere* function of MATLAB is used to calculate the spectral coherence between two adjacent measuring points. The obtained spectral coherence and the fitted curves obtained using the formula given in Yang *et al.* (2022b) are illustrated in Fig. 9. In the figure, C represents the attenuation coefficient, K is the coherence degree of the PSD of two measuring points when the frequency approaches 0, Δ represents the distance between two measuring points, and $\overline{U}$ represents the mean value of the average wind velocity of two sampling points selected. As shown in Fig. 9, the coherence between two adjacent measuring points decreases rapidly with the increase in frequency, whereas the value of K approaches 1 when the frequency approaches 0. The coherence degree between #2 and #3 in the low-frequency band ($K = 0.94$) is slightly higher than that between #1 and #2 ($K = 0.89$). Given that the dominant frequency of the wind field in this site is about 0.008 Hz (corresponding to the horizontal coordinate value of about 0.02 in Fig. 9), the time-history samples of fluctuating wind velocity collected at each of the three measuring points are representative.

III. IDDES-BASED CFD method
A. Overview of the model
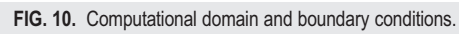#### 1. Geometry domain and boundary conditions

The CFD model considered in the present study has three scales: 1:1, 1:10, and 1:20. Taking the 1:10 scale model as an example, the geometric parameters, boundary conditions, and grid strategy of the model are described below.

Figure 10 illustrates the geometric parameters of the computational domain and the corresponding boundary conditions. The geometric dimensions in the model are nondimensionalized according to the dimensions of the HST (CRH380B, three-carriage grouping). Among them, the longitudinal dimensions are measured by the length

of the head carriage L; the transverse dimensions are measured by the width W; the vertical dimensions are measured by the height H. When the scale ratio is 1:10, the values of L, W, and H are 2.5, 0.327, and 0.389 m, respectively. The windbreak wall on the embankment is solid with its porosity being 0. The porosity of the wind barrier on the bridge is simulated by square holes, and the porosity is 30%. The lengths of the embankment and bridge sections are $5L$ each. The zero point on the X coordinate is the junction of the windbreak wall and wind barrier, which is positive from the embankment to the bridge. Other details of the geometric dimensions are given in Fig. 10. As for the boundary conditions, velocity inlet is applied to the boundary of the incoming flow, symmetry is applied to the top of the computational domain, and no-slip wall is applied to the surfaces of the ground, embankment, windbreak wall, wind barrier, bridge, and train. Pressure outlet is applied to both ends of the computational domain and to the opposite sides of the incoming flow boundary.

2. Computational mesh and solution strategy

Figure 11 shows the corresponding grid model. The whole computational domain is discretized by poly-hexcore mesh cells. The grid model of the train is considered only in the dynamic model (the details of dynamic grid setting can be found in Yang *et al.* (2022b), whereas the train model is not considered in the static model. A total of 10 boundary layers are set on the surfaces of the train, embankment, bridge, as well as the windbreak wall and wind barrier. The corresponding boundary layer parameters are given in the figure, which do not change with the scale ratio of the model. The value of $y^+ < 10$, and the computational time step is set as 1×10^{-4} s. Transient solution is pursued with 20 iterations at each time step. The setting schemes of other computational parameters in line with the IDDES method can be found in Yang *et al.* (2022c). In the embankment–bridge model, a two-layer mesh refinement zone is set up with the junction of the embankment–bridge being the center. Under the 1:10 scale ratio, the mesh size range of the embankments, bridges the windbreak wall and wind barrier is between 0.004 and 0.01 m, and the thickness of the first layer is 0.4–1 mm. The mesh size range of the first

FIG. 10. Computational domain and boundary conditions.

refinement zone is between 0.004 and 0.02 m. The global size of the model ranges from 0.004 to 0.05. The mesh size of 1:1 model and 1:20 model increases or decreases by 10 times. The total number of grid cells in the model is about 45×10^6.

In this study, IDDES turbulence model was used to solve the computational mesh. The IDDES-*SST* model is based on modifying the sink term in the *k-w* of the *SST* model (Shur *et al.*, 2008),

FIG. 11. Mesh model.

$$\frac{\partial \rho k}{\partial t} + \nabla \cdot (\bar{\rho} \tilde{U} k) = \nabla \cdot \left[\left(\mu + \frac{\mu_T}{\sigma_{k3}} \right) \nabla k \right] + P_k - \rho \beta^* k \omega F_{IDDES},$$
(4)

$$\frac{\partial \rho \omega}{\partial t} + \nabla \cdot (\bar{\rho} \tilde{U} \omega) = \nabla \cdot \left[\left(\mu + \frac{\mu_T}{\sigma_{\omega 3}} \right) \nabla \omega \right] + (1 - F_1) 2\rho$$
$$\times \frac{\nabla k \cdot \nabla \omega}{\sigma_{\omega z} \omega} + \alpha_3 \frac{\omega}{k} P_k - \beta_3 \rho \omega^2,$$
(5)

$$F_{IDDES} = \frac{l_{RANS}}{l_{IDDES}},$$
(6)

where $l_{RANS} = \sqrt{k}/(\beta^* \omega)$, F_{IDDES} is based on the Reynolds-averaged Navier-Stokes (RANS) turbulent length scale and the large eddy simulation (LES) grid length scales.

3. Verification

To verify the reliability of the boundary layer scheme and turbulence simulation scheme, the mesh strategy described in Sec. III A 1 was introduced by referring to Maruyama (2008) wind tunnel test setup, and three CFD models were established in accordance with three boundary layer schemes (Fig. 12). In Fig. 12, coarse, medium, and fine indicate generating 5, 10, and 20 grid layers around a fence model, respectively. In the CFD simulation, the incoming flow has a constant wind velocity of 10 m/s, and the computational parameter settings are the same as given in Sec. III A 1. The measuring lines L_1

and L_2 are located on the windward and leeward sides of the fence, respectively, and 0.1 m away from the fence. When the computational result stabilizes, the continuous sampling time is 6 s. Figure 13 provides a comparison of wind velocity distribution results obtained by the three grid schemes and the wind tunnel test results, where the value of wind velocity is the average value of the component along the direction of incoming flow in a 6 s period. It is observed from Fig. 13 that the results of the medium and fine mesh schemes are in good agreement with the experimental results, whereas the deviation of the results of the coarse scheme is slightly larger. The medium grid scheme is reasonably compromising computational cost and accuracy.

B. Result analysis

The sudden change of train aerodynamic load is due to the huge difference in wind field environment between the single solid windbreak wall of embankment and the double-side porous barrier of bridge. The change of train aerodynamic load is inevitable due to the switch of infrastructure during train operation. The average wind speed of incoming flow is the main factor affecting the aerodynamic load of trains. Under high wind speed crosswind, trains will be subjected to higher aerodynamic load. The larger the turbulence intensity of the incoming flow, the fluctuation extent of the train aerodynamic load increases. In addition, a large number of vortices falloff the leeward side of the windbreak wall under the crosswind, which will change the flow field structure around the train and lead to the deterioration of the aerodynamic performance of the train. Therefore, the
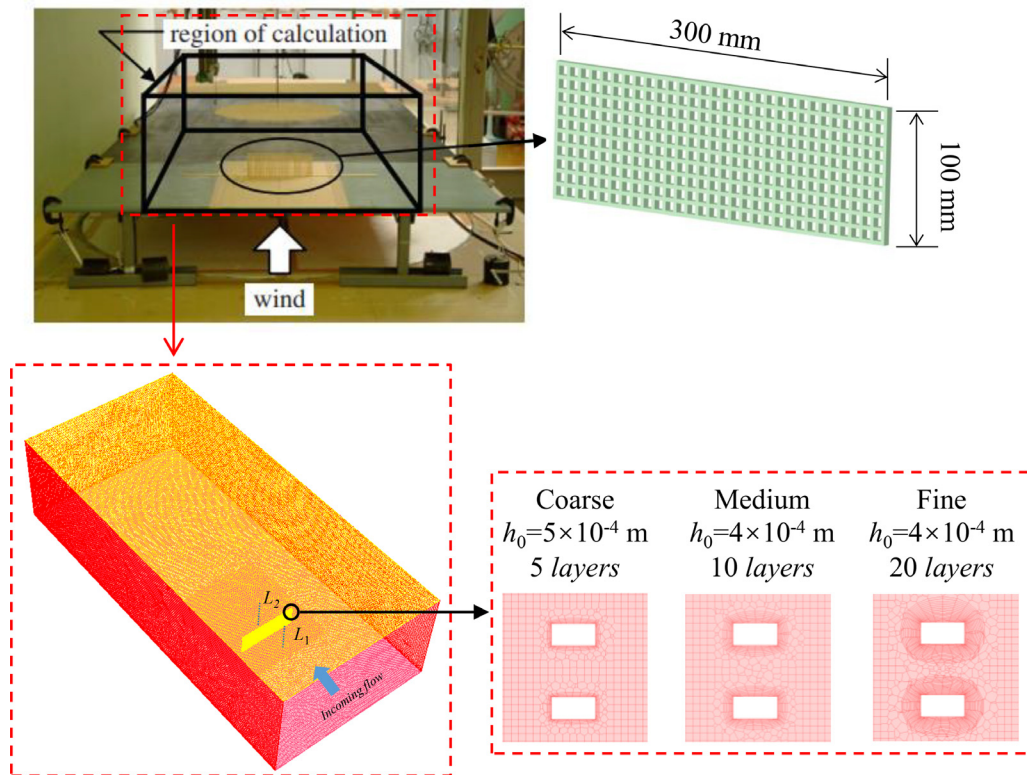

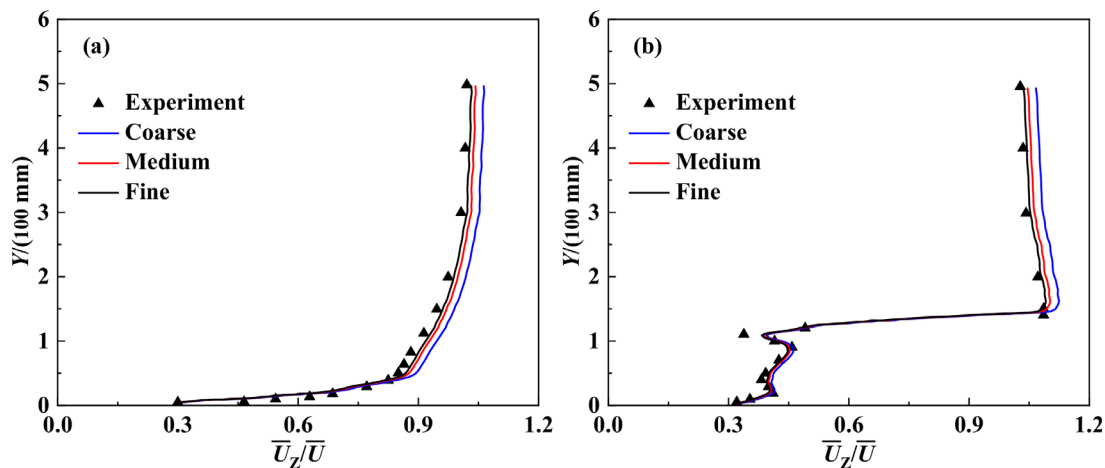**FIG. 12.** Maruyama's wind tunnel test setup and the corresponding grid model.

FIG. 13. Comparison of experimental results and the corresponding numerical results: (a) L_1 and (b) L_2.

mean field, turbulence, and vortex cores are directly related to the aerodynamic behavior of trains (Yang *et al.*, 2022d). Therefore, the premise of studying the change of train aerodynamic load is to study the characteristics of wind field, such as average wind velocity, turbulence intensity, and transient vortex.

1. Time-history of wind velocity

Figure 14 illustrates the wind velocity time-history samples of the U component (corresponding to the Z direction in the CFD model) collected at measuring point #2. As shown in Fig. 14, two samples with a duration of 6 s, i.e., samples 1 and 2, are selected in the time-history in the high- and low-speed segments, respectively. These two samples are, respectively, taken as boundary conditions of incoming flows for subsequent analyses.

Figures 15 and 16, respectively, show the time-history curves of the Z-component wind velocity at measuring points along the Z and X directions under the sample 1 condition calculated by the model with 1:10 scale ratio. Here, $\bar{U}$ is the average wind velocity at the boundary of the corresponding incoming flow, which is 23 m/s under sample 1 and 13.8 m/s under sample 2. The red curve in Fig. 16 represents the time-history of sample 1 input on the corresponding incoming flow boundary.

As shown in Fig. 15, the time-history of wind velocity fluctuation maintains good consistency in the direction of incoming flow. In the
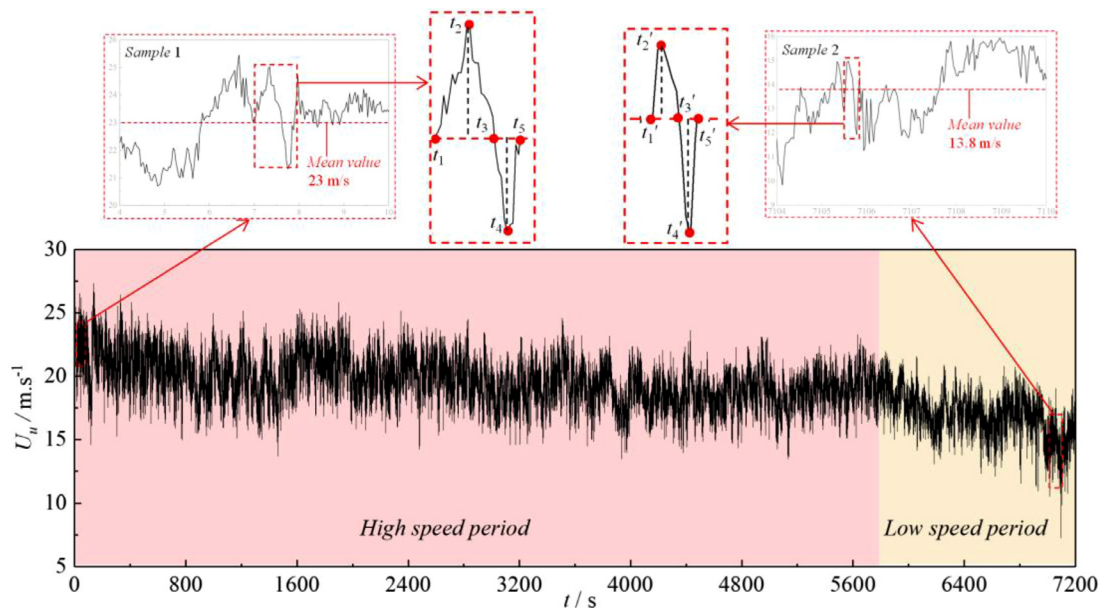

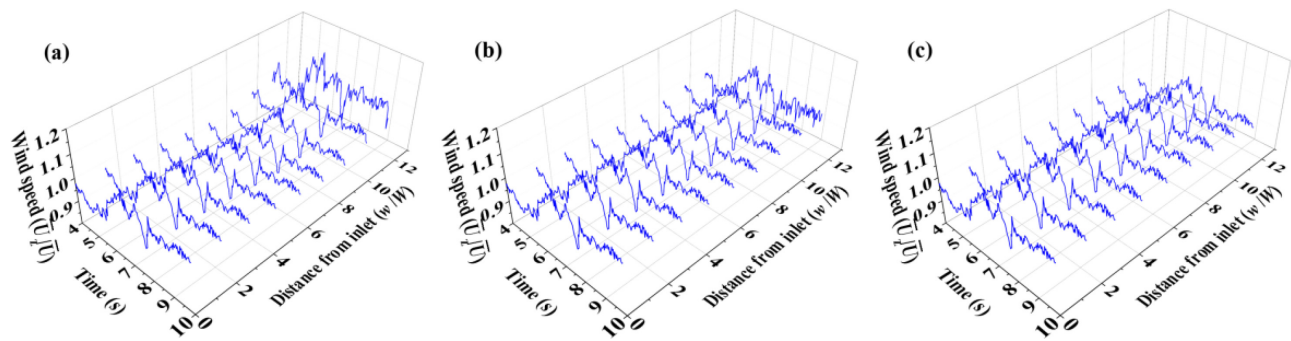**FIG. 14.** Sample selection of the U-component wind velocity.

FIG. 15. Time-history of the Z-component wind velocity on three measuring lines along the Z direction under the sample 1 condition: (a) L_{z1}; (b) L_{z2}; and (c) L_{z3}.

range of 0–7 W, the wind velocity fluctuation amplitude decreases slightly along the positive direction of Z. On the measuring line corresponding to the embankment section, the fluctuation amplitude of wind velocity suddenly increases near the position of the solid windbreak wall due to the windbreak of the incoming flow blocking effect, resulting in flow diversion and acceleration effect. As observed in Fig. 16, the wind velocity fluctuation amplitude on the leeward side of the windproof structure is considerably higher than that of the incoming flow at the boundary. In the embankment section, the wind velocity fluctuation amplitude on the windward and leeward lines is the same, both fluctuating around zero value, and the time-history keeps good synchronization in the longitudinal section. In the bridge section, the wind velocity on the leeward side of the wind barrier increases, and the fluctuation range of wind velocity on the leeward line is considerably higher than that on the windward line, but it is lower than the corresponding value in the embankment section overall.

2. Evolution of transient vortex

Figure 17 shows the evolution process of the transient wake vortex structure on the leeward side of the junction section of the windbreak wall and wind barrier based on the Q-criterion ($Q = 30\,000$) under the conditions of samples 1 and 2, respectively, calculated by the model with a scale ratio of 1:10. Here, the vortex structure is dyed with dimensionless resultant wind velocity; the constant incoming flow indicates the condition that the wind velocity on the inlet boundary is constant as the average wind velocity; the descriptions of typical moments t_1–t_5 and t_1'–t_5' are given in Fig. 14.

It is observed in Fig. 17 that after the incoming flow bypasses the top of the solid windbreak, it generates the acceleration effect and separates into numerous cordlike vortex structures on the leeward side. In the near area of the wall top, the cordlike vortex is parallel to its edge. With the increase in distance, the posture of the vortex structures evolves to be perpendicular to the wall after separation and rupture. Due to inertia, the interaction between vortices leads to the attenuation of turbulent kinetic energy along the incoming flow direction. Therefore, the large vortex on the leeward side of the windbreak wall gradually evolves into a middle vortex, and the middle vortex gradually evolves into a small vortex. The energy on the small-scale vortex is converted into heat and finally dissipated. The number of wake vortices generated under the condition of high-speed incoming flow is remarkably more than that under the low-speed condition, and the
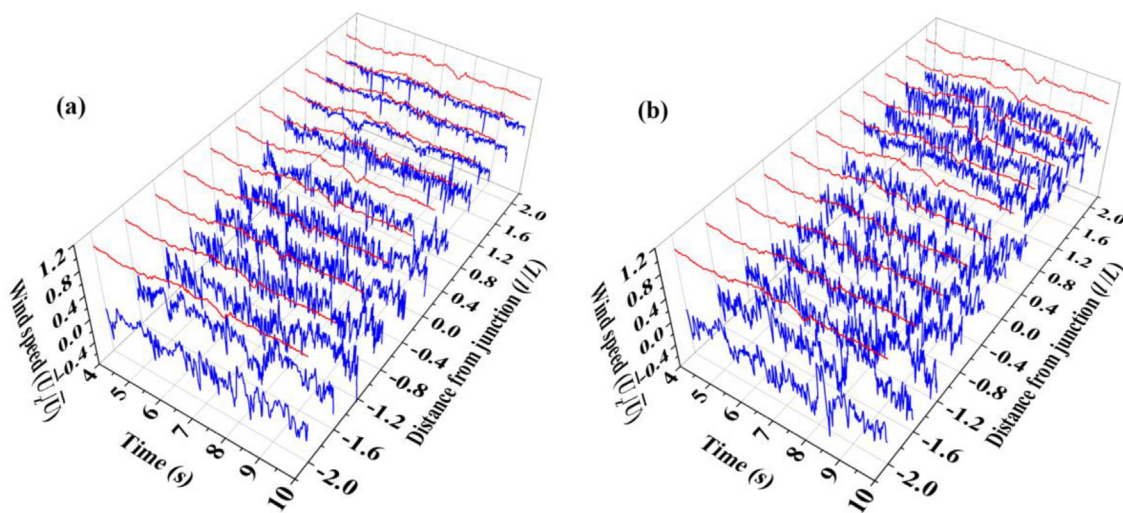

FIG. 16. Time-history of the Z-component wind velocity on two measuring lines along the X direction under the sample 1 condition: (a) L_{x1} and (b) L_{x2}.
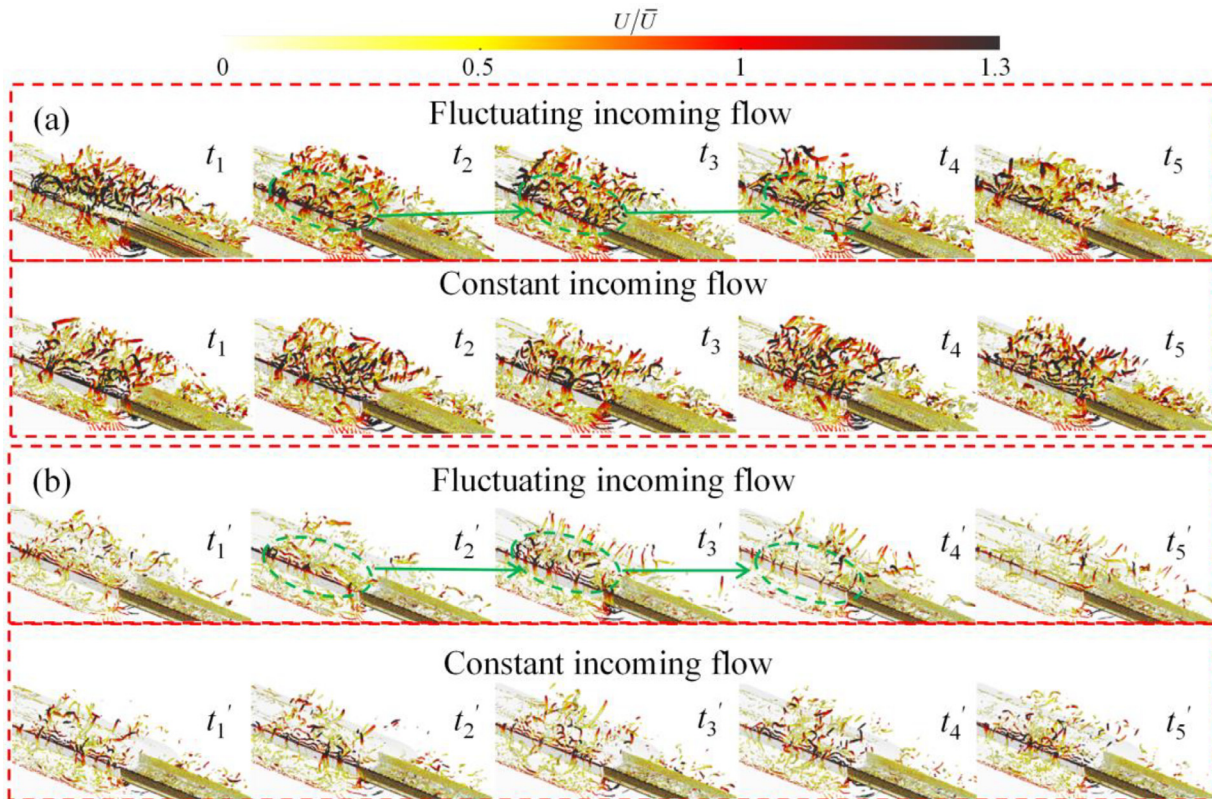
FIG. 17. Evolution process of the wake vortex structure in the transition section of windbreak wall and wind barrier (Q = 30 000): (a) sample 1 and (b) sample 2.

acceleration effect at the top of the windbreak wall is considerably higher than that under the low-speed condition (the maximum dimensionless wind velocity can reach 1.3).

Under the condition of constant incoming flow, the shedding evolution process of the vortex structure on the leeward side of the windbreak wall is relatively stable. While under the condition of fluctuating incoming flow, the time-varying incoming wind velocity evokes the instability of the wake vortex, and this phenomenon is particularly crucial under the condition of low-speed incoming flow. The evolution of wake vortices may be related to the variation of incoming wind velocity. When the fluctuating wind velocity at the inlet boundary reaches its peak (t_2 or t_2'), the corresponding wake flow velocity is not the highest; when the incoming flow velocity decreases (t_3 or t_3'), the wake flow velocity and the number of vortex structures increase; when the incoming flow velocity reaches its trough (t_4 or t_4'), the wake flow velocity and the number of vortex structures decrease. This shows that the evolution of wake vortex structure of the windbreak wall exhibits hysteretic behavior relative to the change of wind velocity at the inlet boundary. However, the above characteristics are not remarkably featured in the bridge section.

3. Average wind velocity

Figure 18 shows a comparison of the distribution curves of the average wind velocity values of the Z-component on three measuring lines along the direction of the incoming flow under the conditions of samples 1 and 2, calculated by the model with a scale ratio of 1:10. As shown in Fig. 18, the distribution characteristic of the average wind velocity along the direction of incoming flow is consistent with that given in Fig. 15, and the attenuation law under the condition of fluctuating incoming flow is consistent with that under the condition of constant incoming flow. On the measuring line corresponding to the embankment section, the average wind velocity attenuation amplitude can reach 5% under the condition of samples 1 and 2. Interestingly, under the condition of sample 1, the wind velocity under the condition of fluctuating incoming flow is slightly higher than its counterpart under the condition of constant incoming flow. However, the two values are consistent under the condition of sample 2. The reason may be that compared with the constant incoming flow condition, the turbulent kinetic energy of the incoming wind is higher under the fluctuating incoming flow condition, and the energy dissipation along the direction of the incoming flow is lower.

Figures 19–21 show the distributions of average wind velocity on the leeward side of the windproof structure under incoming flow conditions of samples 1 and 2, respectively. As illustrated in the figures, in terms of longitudinal distribution, regardless of sample 1 or sample 2, the wind velocity increases sharply at the junction of the windbreak wall and wind barrier. The Z-component of wind direction on the leeward side of the windbreak wall is mainly negative because of the gyro vortex falling off the top of the wall. The Z-component of wind
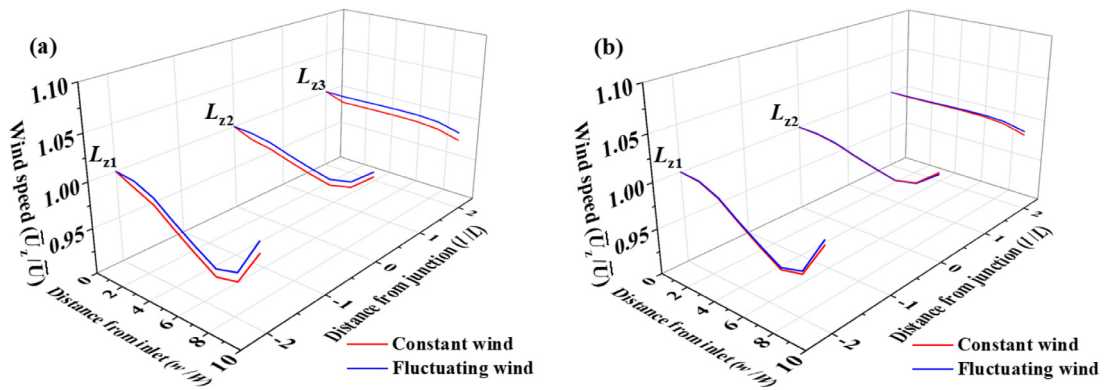
FIG. 18. Average wind velocity distribution curves of the Z-component along three measuring lines in the Z direction: (a) sample 1 and (b) sample 2.
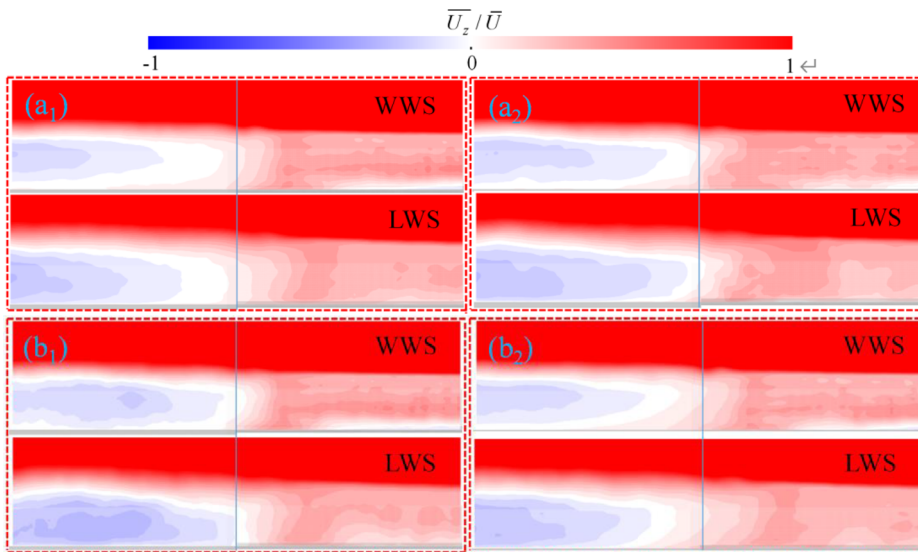

FIG. 19. Z-component mean wind velocity distribution on the central longitudinal section of the windward and leeward lines: (a) sample 1 and (b) sample 2 (subscripts 1 and 2 denote the fluctuating and constant incoming flows, respectively).
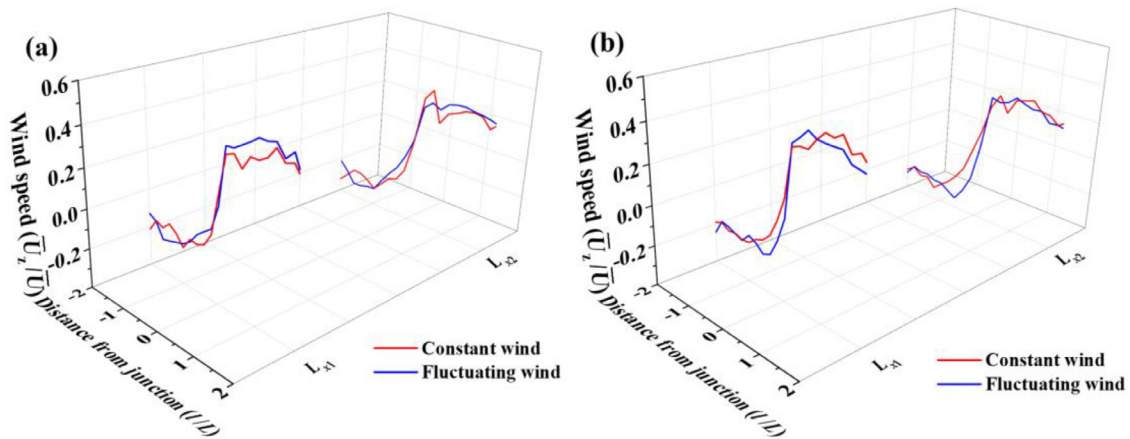

FIG. 20. Average wind velocity distribution curves of the Z-component along two measuring lines in the X direction: (a) sample 1 and (b) sample 2.
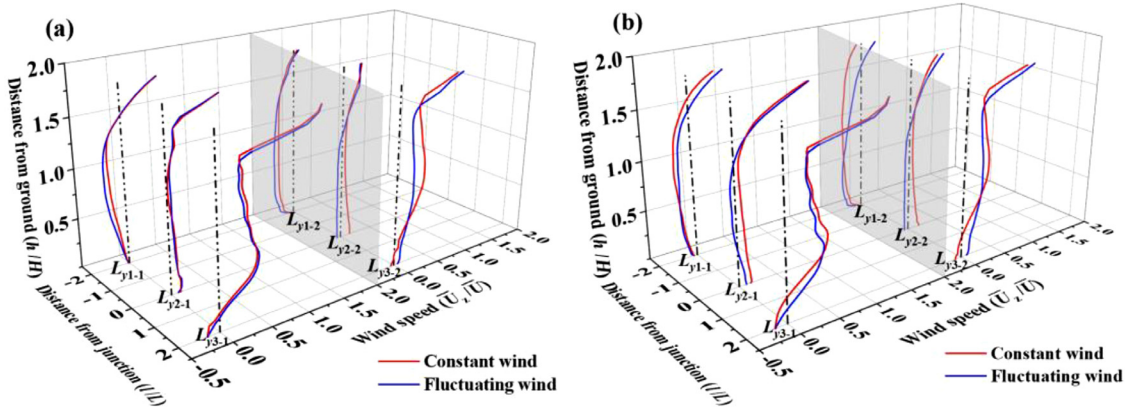
FIG. 21. Average wind velocity distribution curves of the Z-component along six measuring lines in the Y direction: (a) sample 1 and (b) sample 2.

direction on the leeward side of the wind barrier is positive, which is caused by the ventilation holes. This means that when the train runs through this section at high speeds, it will encounter a sudden change of wind environment and thus will be imposed by huge aerodynamic load, which threatens the running safety. The influence of incoming flow conditions on the longitudinal distribution of wind velocity is mainly reflected in the windward line. For example, under the sample 1 condition, the jump amplitude (0.73) under the condition of fluctuating incoming flow is 7.3% higher than its counterpart (0.68) under the condition of constant incoming flow. However, under the sample 2 condition, the jump amplitude under the condition of fluctuating incoming flow (0.69) is 5.5% lower than that under the condition of constant incoming flow (0.73).

The incoming flow condition has a weak effect on the vertical distribution. In terms of vertical distribution, the wind velocity variation amplitude along the windward line is higher than that along the leeward line. At the position of $-2L$, from bottom to top ($1.33H$ corresponding to the wall top), the wind velocity first increases negatively

and then positively. Even, at the height of $1.1H$, the dimensionless wind velocity in the negative direction reaches the highest value (-0.3). At the $2L$ position, the dimensionless wind velocity can reach 0.5 at the height of $0.5H$. The above phenomenon has also been revealed in the study of Gu *et al.* (2020). Regardless of the section (whether in the embankment or bridge section), the wind velocity starts to show remarkable positive increase at the height of $1.5H$ (the area where the catenary is situated). Especially, in the bridge section, the dimensionless value of the wind velocity reaches up to 1.5, indicating that the installation of a wind barrier generates additional wind load acting on the catenary structure.

4. Turbulence intensity

Figure 22 shows the distribution of average turbulence intensity on the central longitudinal section of the windward and leeward lines on the leeward side of the windproof structure under the incoming flow conditions of samples 1 and 2, calculated by the model with a
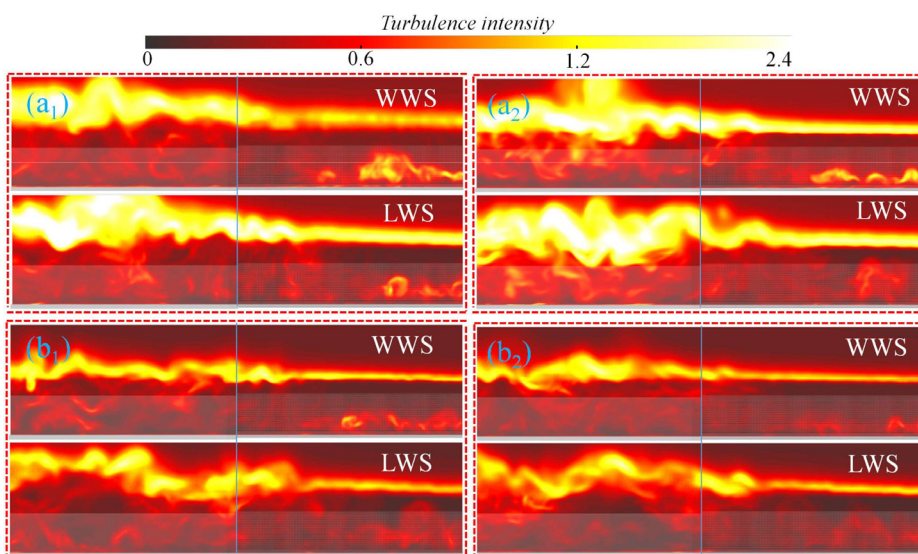

FIG. 22. Average turbulence intensity distribution on the central longitudinal section of windward and leeward lines: (a) sample 1 and (b) sample 2 (subscripts 1 and 2 denote the fluctuating and constant incoming flows, respectively).
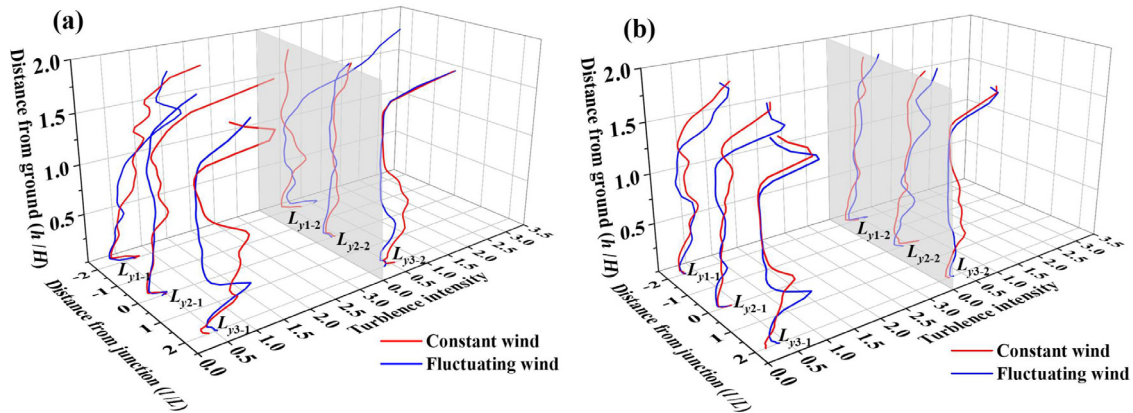
FIG. 23. Average turbulence intensity distribution along six measuring lines in the *Y* direction: (a) sample 1 and (b) sample 2.

scale ratio of 1:10. Figure 23 shows the distribution of turbulence intensity along the corresponding measuring line. As found from Fig. 22, the turbulence intensity in the leeward region of the windproof structure is remarkably higher than the highest turbulence intensity obtained at the position of the inlet boundary (0.16, see Sec. II C 2), indicating that the existence of the windproof structure remarkably increases the intensity of changes in the leeward flow field. This result is consistent with the findings from Fig. 16. In the vertical direction, regardless of the structure (the windbreak wall or wind barrier), a considerably high-turbulence area appears above the top (at the height of 1.5*H*), which is caused by frequent vortex shedding in this area (as shown in Fig. 17). This phenomenon indicates that the wind-induced vibration of the catenary structure in this area will be aggravated by the existence of a windproof structure. In the longitudinal direction, a remarkable difference is observed in the distribution of turbulence intensity between the embankment and bridge sections. The range of high turbulence intensity above the top of the windbreak wall in the embankment section is evidently larger than that in the bridge section.

As shown in Fig. 23, in the region below the top of the windproof structure (1.33*H*), the turbulence intensity on the windward line is about 50% higher than that on the leeward line (sample 1), and the

turbulence intensity under sample 1 is generally higher than that under sample 2. Compared with sample 2, the difference in the vertical distribution of turbulence intensity between fluctuating and constant incoming flows under sample 1 is more remarkable, and the difference is mainly reflected in the corresponding area in the bridge section. For example, Fig. 23(a) shows that the high-turbulence region in the corresponding section of the wind barrier ranges from 0.25*H* to 0.5*H* under the condition of fluctuating incoming flow, whereas the corresponding high-turbulence region ranges from 0.5*H* to 1.0*H* under the condition of constant incoming flow. However, evidence for fluctuating incoming flow is insufficient to indicate higher turbulence intensity of the leeward side of the wind barrier under either sample 1 or sample 2, relative to the constant incoming flow condition.

IV. DISCUSSION ON MODEL SCALING EFFECT
A. Difference in turbulence attenuation

Figure 24 shows the distribution curves of average wind velocity and turbulence intensity of the *Z*-component on L_{z2} under the sample 1 condition, which are calculated by the 1:1, 1:10, and 1:20 models, respectively. It is observed in Fig. 24(a) that the distribution of the average wind velocity along the incoming flow direction is consistent
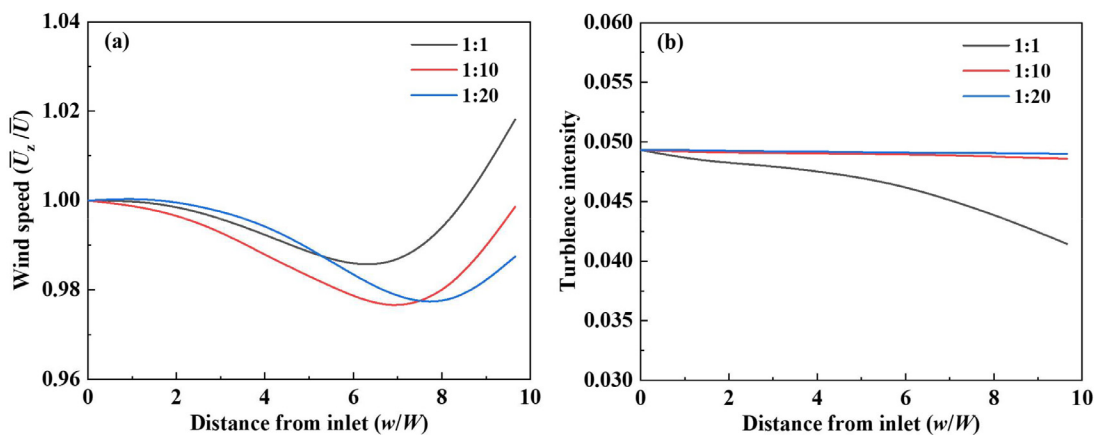
FIG. 24. Distribution curves of the Z-component (a) average wind velocity and (b) turbulence intensity on L_{z2} under the sample 1 condition.

under the three scaling ratios, showing a trend of decreasing first and then increasing (the reason for increase has been revealed in explaining Fig. 15). The 1:1 model reaches the lowest value at 6W away from the inlet boundary, whereas the 1:10 and 1:20 models reach the lowest value at 7 and 7.5W, respectively. According to Fig. 24(b), in the range of 0–10W along the incoming flow direction, the attenuation of turbulence intensity from the 1:10 and 1:20 models is weak, whereas the 1:1 model shows a monotone attenuation trend, with a maximum amplitude of up to 14%.

In summary, the average wind velocity at the boundary of incoming flow can be simulated with acceptable fidelity when a proper reduced-scale model is adopted. As for the turbulence intensity at the boundary of incoming flow, necessary corrections must be performed when using a reduced-scale model.

B. Difference in evolution of transient flow field

Figure 25 shows the evolution process of transient flow field on cross-sections at $-2L$ (embankment) and $2L$ (bridge) obtained by the

1:1, 1:10, and 1:20 models, respectively. In the figure, the cloud diagram color is dyed by the dimensionless transient wind velocity of the Z-component, and the white dotted line marks the larger vortex region. The following findings are obtained from Fig. 25.

In the case of 1:1 model [Fig. 25(a)], the evolution process of flow field structure on the cross-section of the embankment is quite different from that of the bridge section. In the embankment section, the triangular area under the leeward side of the windbreak wall is a gathering area of small vortex structures (its boundary has been marked approximately by a white dotted line in the figure), which mainly covers the windward line. As a result, the turbulence intensity of the wind field on the windward line is higher than that on the leeward line. The shedding and evolution of individual large vortex structures can be observed in the upper area. In the bridge section, the small vortex structures mainly appear in the area near the pavement, and the wind velocity field in the upper area is distributed mainly in the positive direction. In accordance with the changing process of incoming flow velocity [increasing (t_1-t_2) to decreasing (t_2-t_3) and decreasing (t_3-t_4) to increasing (t_4-t_5) in Fig. 14], the boundary line of
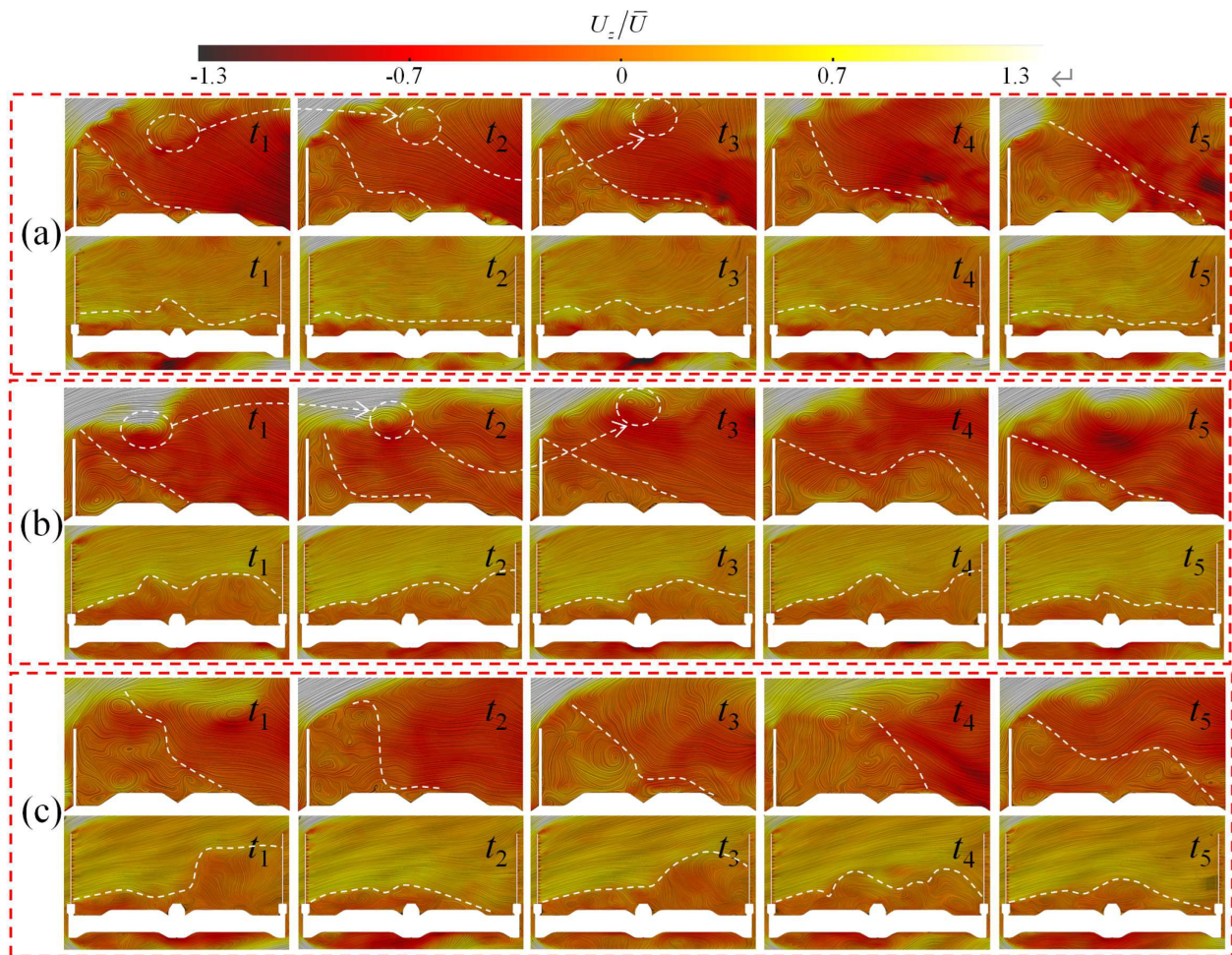

FIG. 25. Evolution process of transient flow field in the leeward side of the windproof structure under fluctuating incoming flow condition of sample 1: (a) 1:1; (b) 1:10; and (c) 1:20.

the small vortex structure gathering area on the leeward side of the windbreak wall in the embankment section exhibits a pattern of "internal concave"–"external convex"–internal concave–external convex (consistent with the hysteretic behavior shown in Fig. 17). However, the evolution of the vortex structure region of flow field in the bridge section is not evident.

In the case of 1:10 model [Fig. 25(b)], the evolution characteristics of the boundary line of the small vortex structures' gathering area in the embankment section along with the wind velocity of the incoming flow are consistent with the law described by the 1:1 model. The shedding evolution process of the large vortex structures can also be observed in the upper area. Compared with the results from the 1:1 model, the gathering area of the small vortices near the pavement in the bridge section is thickened. As for the results obtained by the 1:20 model [Fig. 25(c)], the characteristics of the corresponding transient flow field evolution are largely different from those obtained by the 1:1 model, regardless of section (i.e., in either embankment or bridge section). The specific manifestations are as follows: On the embankment, the gathering area of the small vortices has extended to the leeward line, and its evolution characteristics are largely different from the results presented by the 1:1 model. On the bridge, the small vortex gathering area near the pavement thickens further, and its morphological changes mainly appear on the leeward line.

As regards simulating the transient evolution characteristics of the vortex structures on the leeward side of the windbreak wall, the results obtained by the 1:10 model are in good agreement with the 1:1 model, whereas the results obtained by the 1:20 model have a large deviation.

C. Difference in mean field

The four physical quantities commonly used to describe the flow field are wind velocity, turbulence intensity, turbulence kinetic energy, and vorticity. To compare the prediction performance of the two scale models (1:10 and 1:20) on the wake vortices on the leeward side of the transition section of the windproof structure in terms of the above four quantities, Figs. 26–29, respectively, show the distributions of average wind velocity, turbulence intensity, average turbulence kinetic energy and vorticity calculated by the three scale models on three typical cross-sections under the sample 1 condition. Here, turbulence kinetic energy is dimensionless with respect to the square of the average wind velocity ($\bar{U}^2$) on the corresponding inlet boundary (Wang et al., 2021), and vorticity is dimensionless with respect to H and $\bar{U}$ (Chen et al., 2022b). The following findings can be obtained from Figs. 26–29.

For the average wind velocity (Fig. 26), the distribution characteristics of the average wind velocity on the corresponding cross-section under different scale ratios are consistent. From the embankment section to the bridge section, the average wind velocity in the Z-component on the leeward side of the windproof structure varies from negative to positive (consistent with the results shown in Fig. 19). No remarkable difference is observed between the corresponding results under the conditions of fluctuating and constant incoming flows.

For turbulence intensity (Fig. 27), the difference between the results from different scale models is mainly reflected in the embankment section. In the 1:1 model, a high-turbulence area at the top of the windproof structure and the upper area of the leeward side is observed, and the thickness of this area gradually becomes thinner from the
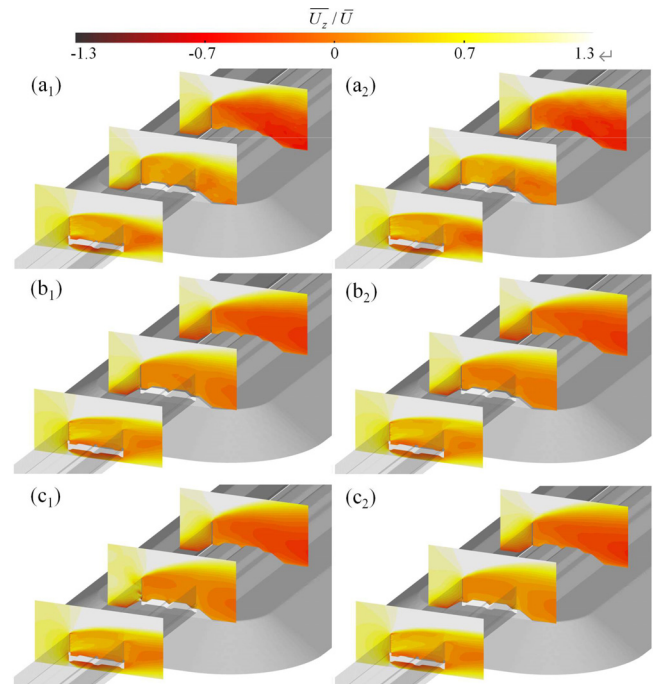

FIG. 26. Average wind velocity distribution of the Z-component on three typical cross-sections under the sample 1 condition: (a) 1:1; (b) 1:10; and (c) 1:20 (subscripts 1 and 2 denote fluctuating and constant incoming flows, respectively).

FIG. 27. Average turbulence intensity field on three typical cross-sections under the sample 1 condition: (a) 1:1; (b) 1:10; and (c) 1:20 (subscripts 1 and 2 denote fluctuating and constant incoming flows, respectively).

FIG. 28. Average turbulence kinetic energy field on three typical cross-sections under the sample 1 condition: (a) 1:1; (b) 1:10; and (c) 1:20 (subscripts 1 and 2 denote fluctuating and constant incoming flows, respectively).
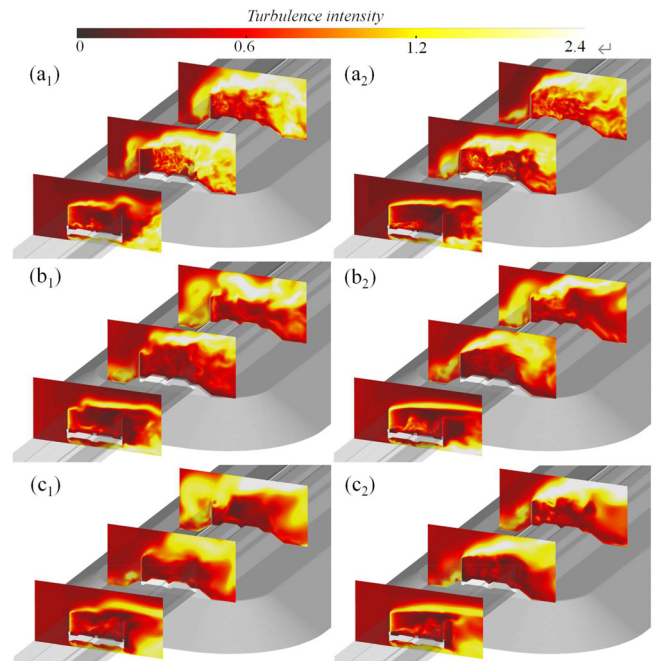

FIG. 29. Average vorticity field on three typical cross-sections under the sample 1 condition: (a) 1:1; (b) 1:10; and (c) 1:20 (subscripts 1 and 2 denote fluctuating and constant incoming flows, respectively).
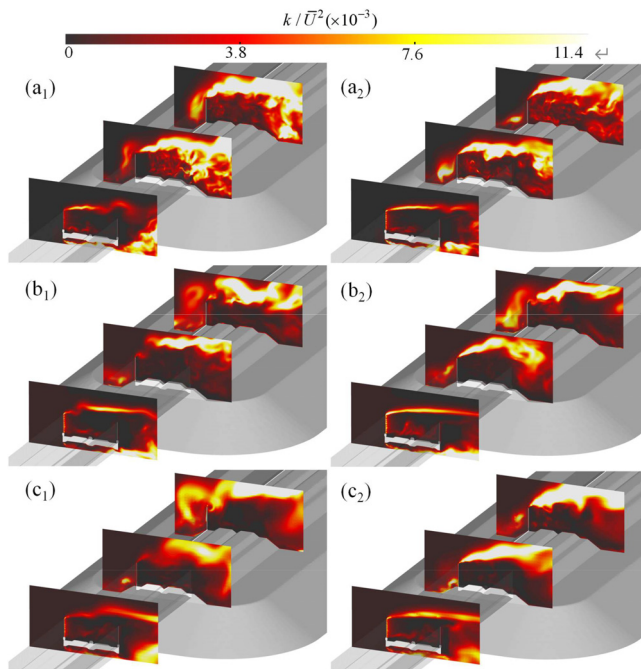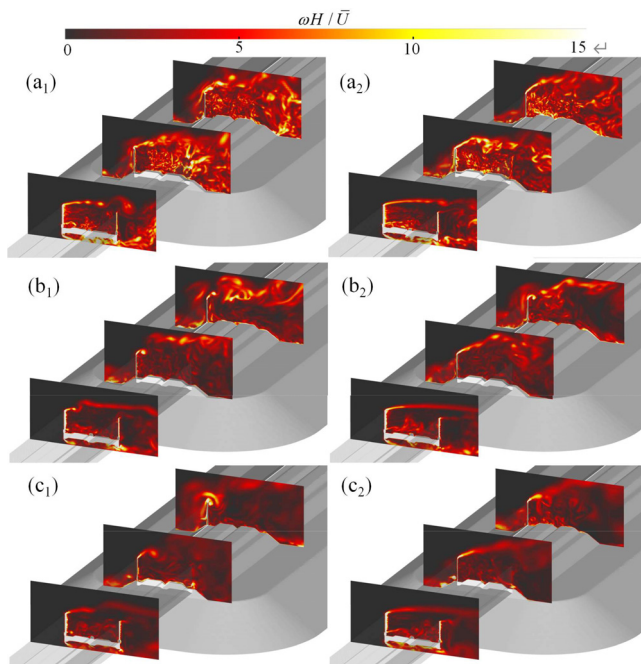
embankment to the bridge (consistent with the characteristics shown in Fig. 22). The thickness of the high-turbulence area under fluctuating incoming flow is slightly larger than that under constant incoming flow. The turbulence intensity on the leeward area of the windproof structure is lower than that on the upper area, and many discrete high-turbulence areas remain on the windward line. In the 1:10 model, the number of high-turbulence areas resolved in the embankment section is reduced. Overall, although its distribution characteristics are still consistent with the results from the 1:1 model, the distribution pattern of the high-turbulence area has changed remarkably. Compared with the turbulence field results from the 1:1 model, the corresponding results from the 1:20 model show great variation. As shown in Fig. 27(c_1), the high-turbulence area at the top of the wind-break wall has spread downward under the condition of fluctuating incoming flow, and the difference between the results and those under the corresponding constant incoming flow condition is further highlighted. For turbulence kinetic energy and vorticity, the difference between the results obtained from different scale models is similar to that on turbulence intensity because both indices depend on the turbulence intensity.

In summary, in terms of simulation performance of the average wind velocity field, the results obtained by the scale models are comparable to those obtained by the full-scale model, and no remarkable difference is observed between the results obtained under the fluctuating and constant incoming flow conditions. In terms of simulation performance of the turbulence field, the results from the 1:20 model show a large deviation. As the scale ratio decreases, the corresponding indicators on the leeward side of the windproof structure decrease, and the difference between the results obtained under the fluctuating and constant incoming flow conditions is gradually highlighted.

D. Difference in PSD

Figure 30 shows the PSD curves of the Z-component wind velocity on the measuring points at $0.5H$ height on measuring lines L_{y1-1}, L_{y2-1}, and L_{y3-1}, calculated by three scale models (1:1, 1:10, and 1:20) under the sample 1 condition. As shown in the figure, the PSD of each measuring point decreases with the increase in frequency. In the case of 1:1 model, the peak PSD in the embankment section [Fig. 30(a_1)] is higher than the corresponding value in the bridge section [Fig. 30(a_3)]. For the wind field on the leeward side of the windbreak wall, the PSD under the condition of fluctuating incoming flow is in good agreement with that under the condition of constant incoming flow. For the wind field on the leeward side of the wind barrier, the high-frequency PSD under the condition of fluctuating wind incoming flow is largely higher than its counterpart under the condition of constant incoming flow. In the case of 1:10 model, the PSD characteristics of the three measuring points and the difference of the results between the constant and fluctuating incoming flow conditions are still in good agreement with the 1:1 model. The peak PSD in the embankment section [Fig. 30(b_1)] is about 10 times higher than the corresponding value in the bridge section [Fig. 30(a_3)]. However, compared with the results of the 1:1 model, the characteristics of the 1:20 model show a large deviation, especially in the bridge section. The specific performance is as follows: in the low-frequency band, the PSD under the condition of fluctuating incoming flow is about 10 times higher than that under the condition of constant incoming flow; in the high-frequency band, the PSD values under the two conditions are consistent.
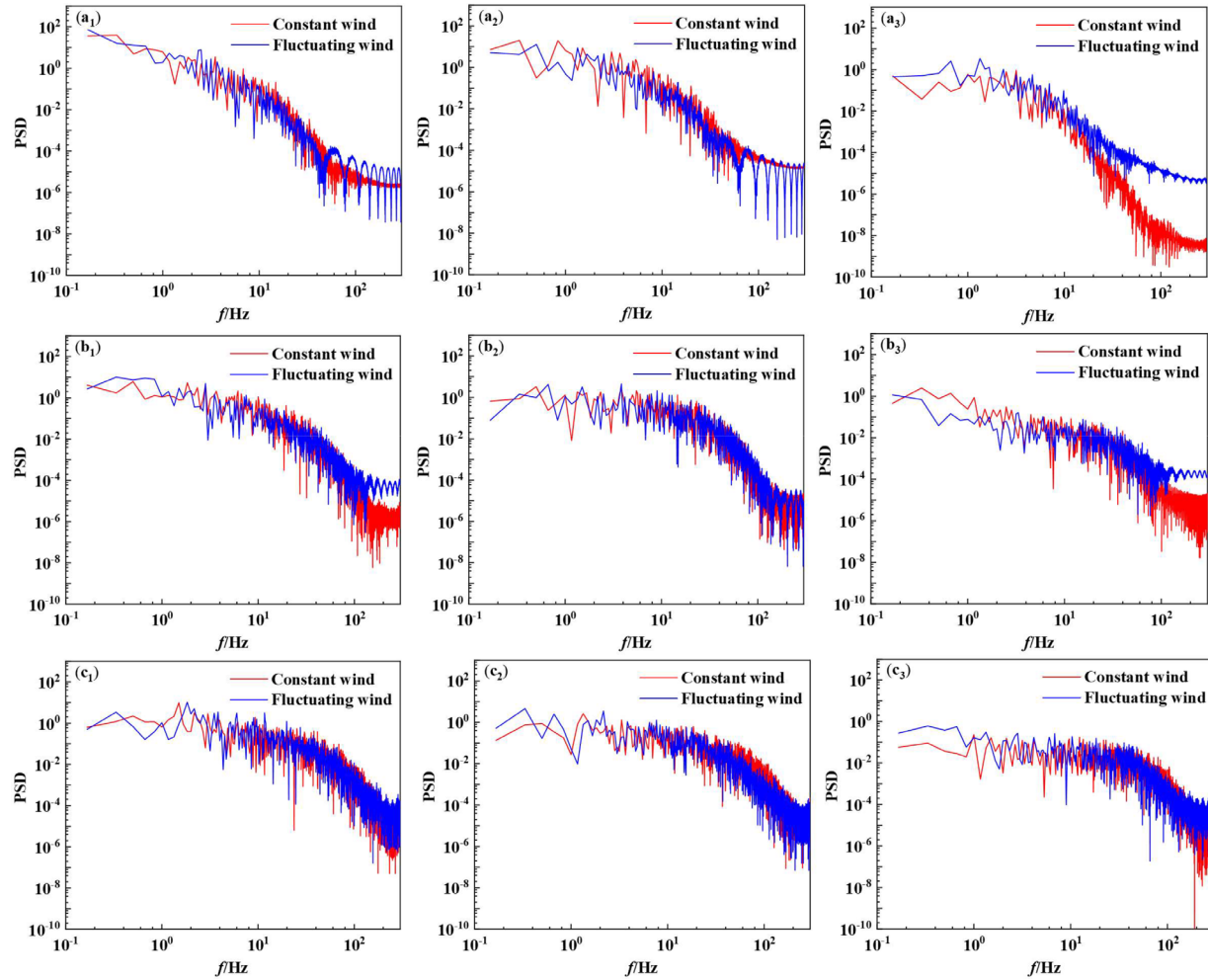
FIG. 30. PSD curves of the Z-component wind velocity at 0.5 H height on windward line under the sample 1 condition: (a) 1:1; (b) 1:10; and (c) 1:20 (subscripts 1, 2, and 3 denote L_{y1-1}, L_{y2-1} and L_{y3-1}, respectively).

V. CONCLUSIONS

Leveraging field tests and numerical simulation by IDDES, a series of analyses were conducted to elucidate the evolution characteristics of the wake vortex of windproof structures on the embankment–bridge transition section along a high-speed railway and to reveal the effect of scaling ratio (1:20, 1:10, and 1:1) on the turbulence field simulation. The main conclusions are as follows:

(1) The incoming wind field in a flat windy area exhibits remarkable two-dimensional characteristics. When the fluctuating wind velocity reaches 25 m/s or above, the representative value of turbulence intensity is 0.03–0.04, and the average turbulence integral scale can reach 350 m.

(2) In the range of 0–$10W$ along the incoming flow direction, the attenuation of the average turbulence intensity obtained from 1:10 and 1:20 models is weak, whereas that from the 1:1 model

can reach 14%. The average wind velocity at the boundary of incoming flow can be simulated with acceptable fidelity when a proper reduced-scale model is adopted.

(3) The average wind velocity along the longitudinal windward line increases sharply at the junction of the windbreak wall and the wind barrier under fluctuating incoming crosswind with high speeds.

(4) The incoming flow with time-varying velocity evokes the instability of wake vortex of the windbreak wall in the embankment, and this phenomenon is particularly crucial under the condition of low-speed incoming flow. The transient evolution results of the vortices obtained by the 1:10 model are in good agreement with the 1:1 model, whereas the results obtained by the 1:20 model exhibit a large deviation.

(5) The results of the average wind velocity field obtained by the scale models are comparable to those obtained by the full-scale

model, and no remarkable difference is found between the results obtained under the fluctuating and constant incoming flow conditions. The results of the turbulence field of the 1:20 model show a large deviation.

In the future research, the wind-vehicle-embankment–bridge CFD dynamic model will be established to study the time-varying regularities of the train's flow field structure and aerodynamic load. What's more, wind-vehicle-embankment–bridge coupling dynamic model will be also established to study the effect of infrastructure switching on dynamic response indexes the train.

AUTHOR DECLARATIONS

Conflict of Interest

The authors have no conflicts to disclose.

Author Contributions

E. Deng: Conceptualization (lead); Data curation (lead); Formal analysis (equal); Investigation (lead); Methodology (lead); Visualization (equal); Writing – original draft (lead). **Huan Yue:** Formal analysis (equal); Investigation (supporting); Software (lead); Validation (lead); Visualization (equal). **Yi-Qing Ni:** Funding acquisition (equal); Project administration (equal); Resources (equal); Supervision (equal); Writing – review & editing (lead). **Xu hui He:** Funding acquisition (equal); Project administration (equal); Resources (equal); Supervision (equal); Writing – original draft (supporting). **Wei chao Yang:** Data curation (supporting); Funding acquisition (equal); Resources (equal); Supervision (equal). **Zheng-Wei Chen:** Validation (supporting); Writing – review & editing (supporting).

DATA AVAILABILITY

The data that support the findings of this study are available from the authors upon reasonable request.

REFERENCES

Bendjebbas, H., El-Hadj, A. A., and Abbas, M., "Numerical simulation of the effect of wind barrier openings on high-speed wind flow around a heliostat field," Appl. Math. Modell. **61**, 443–456 (2018).

Chen, Z. W., Liu, T. H., Yu, M., Chen, G., Chen, M. Y., and Guo, Z. J., "Experimental and numerical research on wind characteristics affected by actual mountain ridges and windbreaks: A case study of the Lanzhou-Xinjiang high-speed railway," Eng. Appl. Comput. Fluid Mech. **14**(1), 1385–1403 (2020).

Chen, Z. W. and Ni, Y. Q., "Sudden flow induced by mountain ridges beside windbreaks in a railway and its mitigation measures," Transp. Saf. Environ. **4**(1), tdac004 (2022a).

Chen, G., Li, X. B., and Liang, X. F., "IDDES simulation of the performance and wake dynamics of the wind turbines under different turbulent inflow conditions," Energy **238**, 121772 (2022b).

Dong, X., Liu, T. H., Shi, Z. L., Xia, Y. T., Yang, F., and Chen, Z. W., "Influence of porosity of reformed earth embankment windbreak wall on flow field and displacement of catenary under crosswinds," J. Wind Eng. Ind. Aerodyn. **214**, 104652 (2021).

Gao, H. R., Liu, T. H., Gu, H. Y., Jiang, Z. W., Huo, X. S., Xia, Y. T., and Chen, Z. W., "Full-scale tests of unsteady aerodynamic loads and pressure distribution on fast trains in crosswinds," Measurement **186**, 110152 (2021).

Gu, H. Y., Liu, T. H., Jiang, Z. W., and Guo, Z. J., "Research on the wind-sheltering performance of different forms of corrugated wind barriers on railway bridges," J. Wind Eng. Ind. Aerodyn. **201**, 104166 (2020).

Hashmi, S. A., Hemida, H., and Soper, D., "Wind tunnel testing on a train model subjected to crosswinds with different windbreak walls," J. Wind Eng. Ind. Aerodyn. **195**, 104013 (2019).

He, X. H., Fang, D. X., Li, H., and Shi, K., "Parameter optimization for improved aerodynamic performance of louver-type wind barrier for train-bridge system," J. Cent. South Univ. **26**(1), 229–240 (2019).

He, X. H. and Li, H., "Review of aerodynamics of high-speed train-bridge system in crosswinds," J. Cent. South Univ. **27**, 1054–1073 (2020).

Hu, P., Han, Y., Cai, C. S., Cheng, W., and Lin, W., "New analytical models for power spectral density and coherence function of wind turbulence relative to a moving vehicle under crosswinds," J. Wind Eng. Ind. Aerodyn. **188**, 384–396 (2019).

Kozmar, H., Procino, L., Borsani, A., and Bartoil, G., "Optimizing height and porosity of roadway wind barriers for viaducts and bridges," Eng. Struct. **81**, 49–61 (2014).

Li, X. Z., Xiao, J., Liu, D. J., Wang, M., and Zhang, D. Y., "An analytical model for the fluctuating wind velocity spectra of a moving vehicle," J. Wind Eng. Ind. Aerodyn. **164**, 34–43 (2017).

Liu, T. H., Chen, Z. W., Zhou, X. S., and Zhang, J., "A CFD analysis of the aerodynamics of a high-speed train passing through a windbreak transition under crosswind," Eng. Appl. Comput. Fluid Mech. **12**(1), 137–151 (2018).

Maruyama, T., "Large eddy simulation of turbulent flow around a windbreak," J. Wind Eng. Ind. Aerodyn. **96**, 1998–2006 (2008).

Masoud, M. and Mohammad, A. R., "Analysis of the effects of lateral wind on a high speed train on a double routed railway track with porous shelters," J. Wind Eng. Ind. Aerodyn. **184**, 116–127 (2019).

Niu, J. Q., Zhou, D., and Liang, X. F., "Experimental research on the aerodynamic characteristics of a high-speed train under different turbulence conditions," Exp. Therm. Fluid Sci. **80**, 117–125 (2017).

Niu, J. Q., Zhou, D., and Wang, Y. M., "Numerical comparison of aerodynamic performance of stationary and moving trains with or without windbreak wall under crosswind," J. Wind Eng. Ind. Aerodyn. **182**, 1–15 (2018a).

Niu, J. Q., Zhou, D., Liang, X. F., Liu, S., and Liu, T. H., "Numerical simulation of the Reynolds number effect on the aerodynamic pressure in tunnels," J. Wind Eng. Ind. Aerodyn. **173**, 187–198 (2018b).

Niu, J. Q., Zhang, Y. C., Li, R., Chen, Z. W., Yao, H. D., and Wang, Y. M., "Aerodynamic simulation of effects of one- and two-side windbreak walls on a moving train running on a double track railway line subjected to strong crosswind," J. Wind Eng. Ind. Aerodyn. **221**, 104912 (2022).

Noguchi, Y., Suzuki, M., Baker, C., and Nakade, K., "Numerical and experimental study on the aerodynamic force coefficients of railway vehicles on an embankment in crosswind," J. Wind Eng. Ind. Aerodyn. **184**, 90–105 (2019).

Shur, M., Spalart, P., Strelets, M., and Travin, A., "A hybrid RANS-LES approach with delayed-DES and wall-modelled LES capabilities," Int. J. Numer. Methods Fluids **29**(6), 1638–1649 (2008).

Telenta, M., Duhovnik, J., Kosel, F., and Sajn, V., "Numerical and experimental study of the flow through a geometrically accurate porous wind barrier model," J. Wind Eng. Ind. Aerodyn. **124**, 99–108 (2014).

Wang, W., Cao, Y., and Okaze, T., "Comparison of hexahedral, tetrahedral and polyhedral cells for reproducing the wind field around an isolated building by LES," Build. Environ. **195**, 107717 (2021).

Wei, L., Zeng, J., Gao, H., and Qu, S., "On-board measurement of aerodynamic loads for high-speed trains negotiating transitions in windbreak walls," J. Wind Eng. Ind. Aerodyn. **222**, 104923 (2022).

05 April 2024 04:48:54

Xu, M., Patruno, L., Lo, Y.-L., and Miranda, S. D., "Simulation strategies for wind shields and porous barriers for bridge deck optimization," Structures **40**, 824–839 (2022).

Yang, W. C., Yue, H., Deng, E., He, X. H., Zou, Y. F., and Wang, Y. W., "Comparison of aerodynamic performance of high-speed train driving on tunnel-bridge section under fluctuating winds based on three turbulence model," J. Wind Eng. Ind. Aerodyn. **228**, 105081 (2022a).

Yang, W. C., Liu, Y. K., Deng, E., He, X. H., Lei, M. F., and Zou, Y. F., "Comparative study on the wind characteristics of tunnel-bridge and tunnel-flat ground infrastructures on high-speed railway," J. Wind Eng. Ind. Aerodyn. **226**, 105006 (2022b).

Yang, W. C., Ouyang, D. H., Deng, E., Wang, Y. W., Chen, Z. W., He, X. H., and Huang, Y. M., "Deterioration of aerodynamic performance of a train driving through noise barriers under crosswinds," J. Wind Eng. Ind. Aerodyn. **231**, 105241 (2022c).

Yang, W. C., Yue, H., Deng, E., Wang, Y. W., He, X. H., and Zou, Y. F., "Influence of the turbulence conditions of crosswind on the aerodynamic responses of the train when running at tunnel-bridge-tunnel," J. Wind Eng. Ind. Aerodyn. **229**, 105138 (2022d).

05 April 2024 04:48:54